The 9th European Congress on Computational Methods in Applied Sciences and Engineering
ECCOMAS Congress 2024
3–7 June 2024, Lisboa, Portugal

PREDICTION OF DUCTILE DAMAGE UNDER VARIOUS SHEAR LOW–CYCLE LOADINGS

Zhichao Wei[1], Steffen Gerke[1] and Michael Brünig[1]

[1] Institut für Mechanik und Statik
Universität der Bundeswehr München
Werner-Heisenberg-Weg 39, D-85577 Neubiberg, Germany
e-mail: zhichao.wei@unibw.de

Key words: Low–cycle ductile damage and fracture, Anisotropic damage model, Numerical simulation, Biaxial experiment, Mixed damage mechanism

Summary. This paper deals with anisotropic ductile damage and fracture behavior under low positive stress triaxialities. Novel tension–shear biaxial low–cycle experiments with different numbers of loading cycles (up to twenty) have been performed using a cruciform biaxially loaded specimen. During the experiment, a tensile preload is first imposed on the horizontal axis until it reaches 3 kN; then, it is kept constant while different shear cyclic loading sequences are superimposed on the vertical axis until failure. All cyclic loadings are driven to a large strain range to investigate ductile damage, and the same amplitude is maintained for each repeated reverse loading cycle within a single loading pattern. In addition, numerical simulations are performed with an anisotropic stress-state-dependent plastic-damage continuum model, also considering the Bauschinger effect. The experimental and numerical analysis of the evolution of the first principal total strain and damage strains highlights the influence of the cyclic loading history on the material behavior. Moreover, fracture surfaces are examined by scanning electron microscopy to analyze the different mechanical performances at the micro-level.

1 Introduction

Damage alters the material matrix at a microscopic level through the nucleation, growth, and coalescence of micro-defects, also leading to degradation of elastic behavior. Ductile damage typically occurs under large plastic deformations, while fatigue damage results from significant strain localization across a large number of loading cycles but within a small strain range [1–4]. Previous literature has focused mainly on ductile damage under monotonic loading conditions. However, some researchers have highlighted how reverse loading conditions can influence the development of ductile damage processes [5–9]. These experiments are characterized by large strain ranges and only few loading cycles, distinctly different from fatigue damage mechanisms. In addition, most of the research mentioned above is restricted to discussing uniaxial cyclic loading conditions with tension-compression or shear experiments. Recently, Wei et al. developed a series of single-cyclic and bi-cyclic biaxial reverse experiments containing only 1.5 loading cycles [10–12]. This method involved altering the loading direction twice, either for one axis or both biaxial axes, during the experiments. Considering various load ratios, these innovatively designed biaxial experiments expanded the range of stress triaxialities from -0.6 to 0.8. Furthermore, the corresponding experimental and numerical results have underscored the

importance of considering reverse loading conditions in analyzing damage and fracture behavior, which is essential for analyzing the life service of engineering structures. Compared to previous studies, this research uniquely employs four different loading patterns, with one, two, six, and twenty complete loading cycles, to demonstrate the impact of cycle number on material mechanical response. Additionally, a mixed damage mechanism, caused by both micro-voids and micro-shear-cracks under low positive stress triaxialities, facilitates the investigation of potential alterations in micro-voids and shear-cracks under reverse loading conditions. Thus, this paper introduces newly designed single-cyclic shear reverse experiments, each superimposed with a 3 kN tensile preload and incorporating various loading cycles.

Numerical calculations are based on a phenomenological anisotropic cyclic plastic-damage model [10, 11]. Unlike the Gurson-type damage model [13–15], the proposed model can describe the degradation of elastic properties. For the proposed material model, the plastic yield condition characterizes the onset of plasticity, and the plastic flow rule models the evolution of inelastic strains due to plastic behavior. Similarly, the damage is characterized by damage condition, and the damage evolution equation accounts for the further development of inelastic strains. Moreover, combined hardening and softening laws are proposed to capture the changes in the plastic yield and damage surfaces more accurately. Previous studies have demonstrated the capability of the proposed material model to accurately simulate various complex loading conditions at both macro- and micro-levels. A brief summary of the constitutive model is described in Section 2. Additionally, Section 3 discusses the experimental loading patterns and their corresponding experimental results. Section 4 compares the experimental and numerical results, while Section 5 concludes.

2 Constitutive modeling

The first stress invariant $\bar{I}_1$ is introduced into the von Mises yield condition to characterize the onset of yielding, taking into account the influence of hydrostatic stress [8]

$$f^{\mathrm{pl}} = \sqrt{\frac{1}{2}\mathrm{dev}(\bar{\mathbf{T}} - \bar{\boldsymbol{\alpha}})\cdot\mathrm{dev}(\bar{\mathbf{T}} - \bar{\boldsymbol{\alpha}})} - \bar{c}\left(1 - \frac{a}{\bar{c}}\,\mathrm{tr}(\bar{\mathbf{T}} - \bar{\boldsymbol{\alpha}})\right) = \sqrt{\bar{J}_2} - \bar{c}(1 - \frac{a}{\bar{c}}\bar{I}_1) = 0\,, \tag{1}$$

where $\frac{a}{\bar{c}}$ describes the hydrostatic coefficient, $\bar{J}_2$ denotes the second deviatoric reduced stress invariant, $\bar{\mathbf{T}}$ is the effective Kirchhoff stress tensor, calculated by the isotropic Hooke's law, and $\bar{\boldsymbol{\alpha}}$ is the effective back stress tensor, capturing the transformation of the yield surface. The three-term decomposed Chaboche's kinematic hardening law [16] has been modified by incorporating an exponential decay and an angle parameter that accounts for activating the nonlinear recovery term in the respective back stress rate tensor [8, 10]. This modification better predicts material behavior under large deformations for the investigated ductile aluminum alloy. In addition, $\bar{c}$ represents the current equivalent stress, governed by the nonlinear double-term Voce hardening law [8]. The modified Voce hardening law enables accurate characterization of the elastic-plastic transition.

A non-associated plastic flow law is used, based on the assumption that there is no volume change in the material due to plastic strain

$$\dot{\bar{\mathbf{H}}}^{\mathrm{pl}} = \dot{\lambda}\frac{1}{2\sqrt{\bar{J}_2}}\,\mathrm{dev}(\bar{\mathbf{T}} - \bar{\boldsymbol{\alpha}}) = \dot{\gamma}\bar{\mathbf{N}}\,, \tag{2}$$

where $\dot{\lambda}$ describes a non-negative multiplier, $\dot{\gamma}$ represents the equivalent plastic strain rate, and

$\bar{\mathbf{N}}$ is the normalized deviatoric reduced stress tensor, which indicates the direction of the plastic strain increment.

The damage condition depends on the stress-state and the first and second reduced stress invariants (I_1 and J_2), which is given by

$$f^{\mathrm{da}} = \hat{\alpha}\,\mathrm{tr}(\mathbf{T}-\boldsymbol{\alpha}) + \hat{\beta}\sqrt{\frac{1}{2}\mathrm{dev}(\mathbf{T}-\boldsymbol{\alpha})\cdot\mathrm{dev}(\mathbf{T}-\boldsymbol{\alpha})} - \tilde{\sigma} = \hat{\alpha}I_1 + \hat{\beta}\sqrt{J_2} - \tilde{\sigma} = 0\,, \tag{3}$$

where $\hat{\alpha}$ and $\hat{\beta}$ are stress-state-dependent coefficients, formulated based on the stress triaxiality and the stress Lode parameter [10], respectively. $\tilde{\sigma}$ describes the current equivalent stress. $\boldsymbol{\alpha}$ denotes the damage back stress tensor which is used to capture the transformation of the damage surface. $\mathbf{T}$ is the Kirchhoff stress tensor, which is formulated by incorporating the damage strain tensor $\mathbf{A}^{\mathrm{da}}$ into isotropic Hooke's law [18,19]. In addition, the damage strain rate tensor is computed in the form

$$\dot{\mathbf{H}}^{\mathrm{da}} = \dot{\mu}(\tilde{\alpha}\frac{1}{\sqrt{3}}\mathbf{1} + \tilde{\beta}\tilde{\mathbf{N}})\,, \tag{4}$$

where $\tilde{\alpha}$ and $\tilde{\beta}$ are stress-state-dependent variables, see [10]. $\mathbf{1}$ is the second order identity tensor and $\tilde{\mathbf{N}}$ represents the transfer deviatoric normalized reduced stress tensor. Thus, the proposed damage evolution equation has the capability of simulating the growth of micro-voids and micro-shear-cracks by considering various combinations of $\tilde{\alpha}$ and $\tilde{\beta}$ under a wider range of stress triaxialities.

3 Experiments

In this work, the biaxially loaded HC-specimen with a thickness of 4 mm is used. In addition, the digital image correlation technique is used to record and analyze the change of deformations for the designed experiments. The geometry and DIC setups are detailed in [17]. The basic loading pattern is similar to that of the single-cyclic shear experiments, as detailed in [10]. Shear cyclic loads are applied to the vertical axis (axis 1), and a constant tensile load of 3 kN is imposed on the horizontal axis (axis 2), as illustrated in Fig. 1(a). The novelty of this paper lies in the range of loading cycles performed in the experiments, i.e., specifically, one, two, six, and twenty cycles, to study damage and fracture behavior under various low-cycle loading conditions. The measurement points used in the experiments and numerical simulations are shown in Fig. 1(b). Mean forces are used because the forces measured from the same axis but different arms (as $F_{i.1}$ and $F_{i.2}$ in Fig. 1(b)) differ slightly, such as $F_1 = \frac{1}{2}(F_{1.1} + F_{1.2})$. In addition, relative displacements u_{ref} between two measurement points are used to characterize the changes in deformation.

The overview of experimental force–displacement curves in axis 1 (vertical axis) is shown in Fig. 2. Noticeably, the forces on axis 2 (horizontal axis) remain constant $F_2 = 3\,\mathrm{kN}$ and are therefore not plotted in Fig. 2. It can be observed that the force–displacement curves align well with the loading cases before the change of loading directions, indicating that the geometry and material show no significant differences due to the specimen manufacturing process. Additionally, the experimental setups provide stable and reliable conditions. The first reverse point depends on the designed loading cycle, as observed in Fig. 1, where the changes in the first loading direction occur at displacements of 0.75 mm, 0.61 mm, 0.53 mm, and 0.41 mm, respectively. The respective maximum equivalent plastic strains γ on the notch surfaces are 0.21,

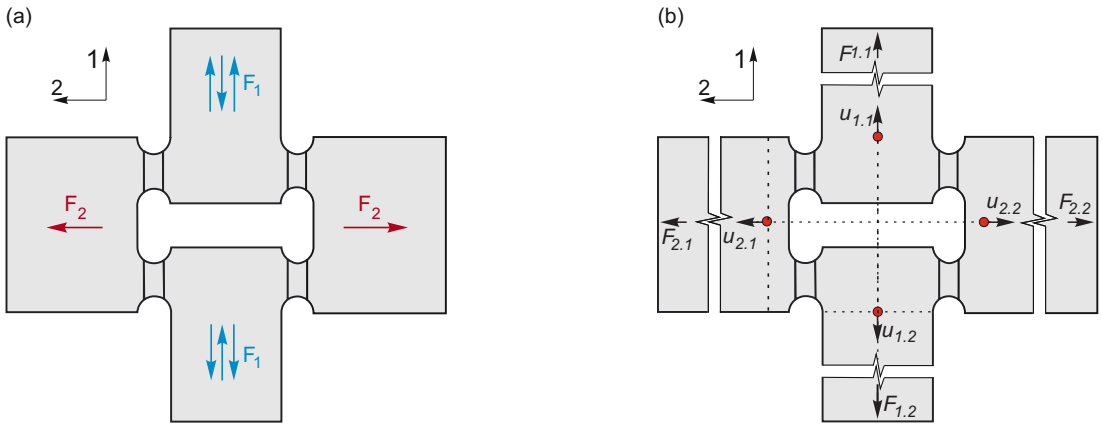

Figure 1: Schematic loading sketch (a) and measure points (b).

0.17, 0.14, 0.11. This is because the greater the plastic deformation prior to reverse loading, the more challenging it becomes to apply a large number of loading cycles experimentally. It is obvious that different fracture forces and displacements are measured during the experiments. The experiment with one full loading cycle failed at a displacement of 0.64 mm with the largest fracture force 4.98 kN. As the number of loading cycles increased, the fracture forces decreased, i.e., the fracture forces for the experiments with two, six, and twenty cycles are 4.78 kN, 4.64 kN, and 4.65 kN, respectively. On the other hand, as the number of loading cycles increases, the difference between the maximum positive forces at the positive loading patterns (except the final fracture forces) and those at the first reverse points gradually decreases. For example, in the

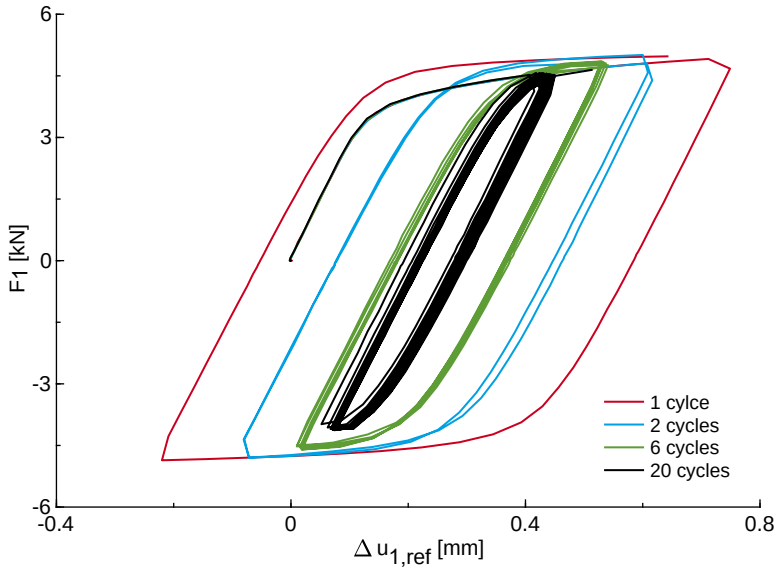

Figure 2: Experimental force–displacement curves.

experiments with only two loading cycles, the maximum forces in the positive loading patterns

are 5 kN at the first reverse point and 4.8 kN at the third reverse point, differing by about 4%. The differences are 1.9% and 1.3% for the experiments with six and twenty cycles, respectively. In addition, the maximum negative forces also vary within each loading pattern, as shown in Fig. 2. These observations may mainly be caused by the plastic deformation applied before the first reverse point, with previous plastic loading histories affecting subsequent plastic behavior, especially the Bauschinger effect.

Although the same relative machine displacements are imposed along axis 1 during experiments for each loading pattern, the resulting force–displacement curves align with each other but slightly shift to the right. Therefore, the force–displacement curves for the experiments with six and twenty loading cycles overlap, creating curves with a certain width, as seen in Fig. 2.

4 Results

The numerical force–displacement curves agree well with the experimental ones before the first reverse point, but exhibit only slight differences between the experimental and numerically predicted fracture forces, as shown in Fig. 3. For example, the simulated fracture force for the

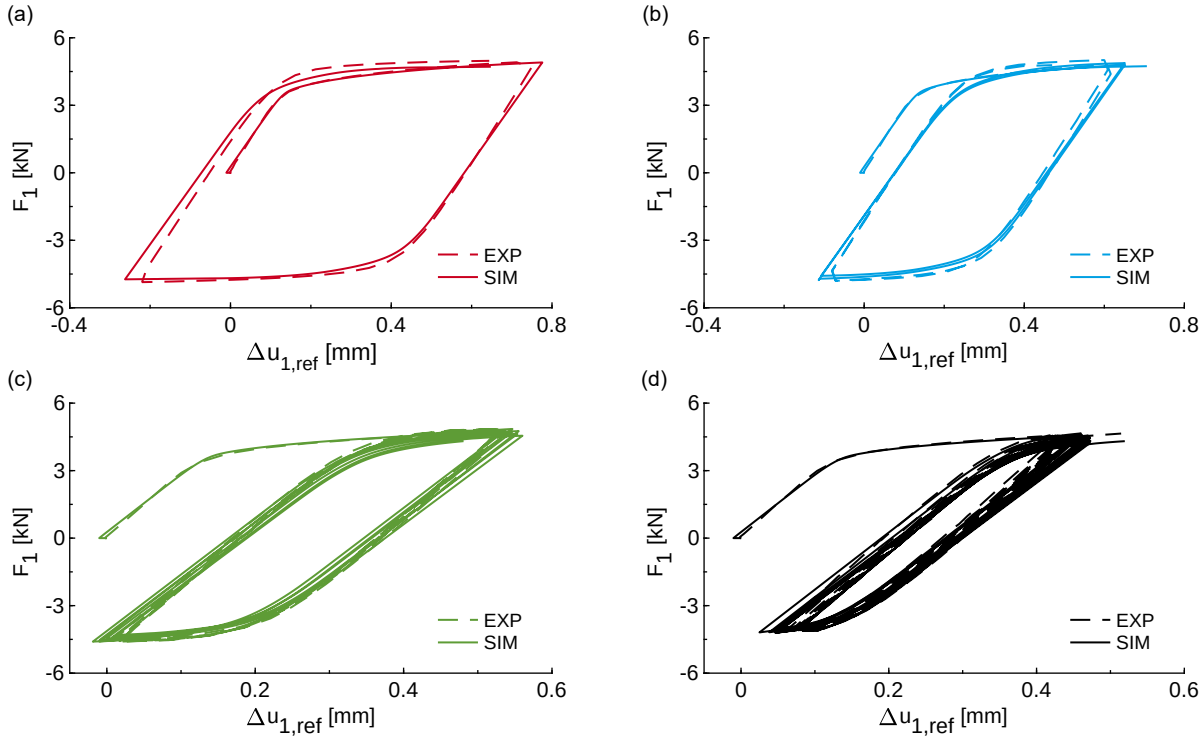

Figure 3: Numerical and experimental force—displacement curves: (a) one cycle, (b)two cycles, (c) six cycles, and (d) twenty cycles.

experiment with one full loading cycle is 4.71 kN, which is smaller than the experimental fracture force of 4.98 kN. Moreover, the fracture forces differ by about 7% between the experiment and numerical prediction for the test containing twenty loading cycles. In addition, the numerically predicted maximum forces at reverse points, where the loading direction changes from shear in tension to shear in compression directions, decrease with an increase in the number of loading

cycles. Conversely, the experimentally observed forces show only slight changes. As observed in the experiments with six cycles, the numerically predicted positive maximum forces are 4.76 kN (1st reverse point), 4.85 kN (at 3rd reverse point), 4.76 kN (5th reverse point), 4.70 kN (7th reverse point), 4.63 kN (9th reverse point), 4.55 kN (11th reverse point), and 4.31 kN (fracture point), respectively, whereas the experimentally measured forces are 4.84 kN, 4.85 kN, 4.84 kN, 4.80 kN, 4.76 kN, and 4.64 kN. It is evident that the proposed material model needs further modification to accommodate multiple changes in loading directions, particularly for a larger number of loading cycles. This modification would accurately reflect how the hardening rate changes with increasing loading cycles [10, 20, 21].

A comparison between the experimentally measured and numerically predicted first principal strains A_1 just before failure on the notch surfaces is depicted in Fig. 4. The numerical results agree well with the experimental ones regarding the shapes of the shear band and the maximum values of A_1. It can be observed that the maximum values of A_1 are localized at the top and bottom of the shear bands. As the number of loading cycles increases, the resulting shear band becomes more distorted, and the maximum values of A_1 show a decreasing trend: 0.27, 0.27, 0.25, 0.24. In addition, as illustrated in Fig. 5, the numerically predicted equivalent plastic strains γ for the experiments with one, two, six, and twenty loading cycles are 0.84, 0.93, 1.15, and 1.35, respectively. These maximum values of γ are observed in the middle of the shear bands on the notch surfaces. The findings above indicate that while the maximum A_1 decreases, the accumulated γ increases with increasing loading cycles.

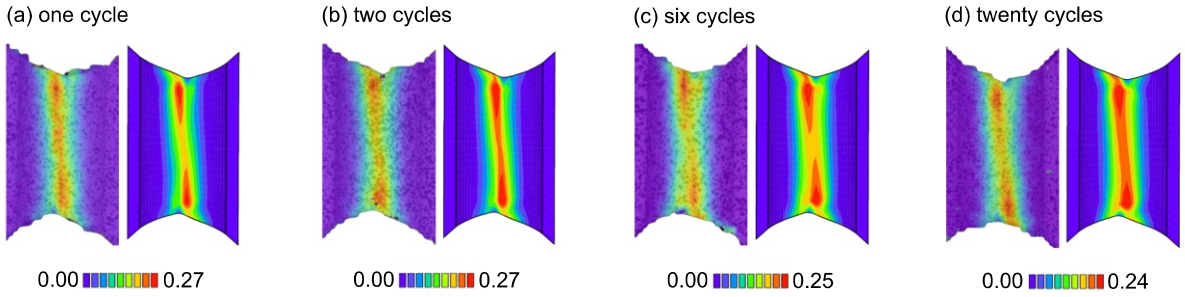

Figure 4: Experimental and numerically predicted first principal strains A_1 on the notch surfaces.

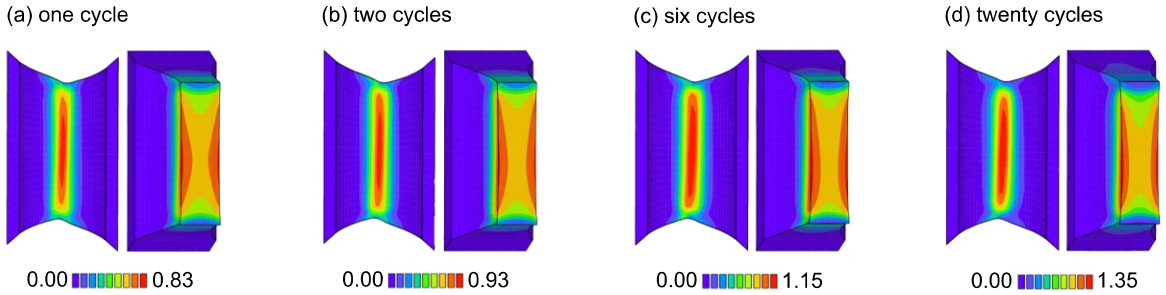

Figure 5: Numerically predicted equivalent plastic strain γ on the notch surface and notched cross-sections.

Moreover, the stress triaxialities η, defined as the ratio of mean stress to equivalent stress, are 0.27, 0.29, 0.26, and 0.25 for experiments with one, two, six, and twenty loading cycles, respectively. The corresponding respective Lode parameters are -0.17, -0.17, -0.30, and -0.29. It is evident that the stress triaxialities change only slightly for experiments with different loading cycles, whereas the Lode parameters show more sensitivity, particularly between two and six loading cycles. On the other hand, the damage strain tensor $\mathbf{A}^{\mathrm{da}}$ characterizes the changes in micro-defects. Accordingly, the distributions of the first principal damage strain A_1^{da} just before failure on the notch surfaces and notched cross-section are demonstrated in Fig. 6. The maximum values of A_1^{da} are numerically predicted at the top and bottom of the shear band on the notch surface, corresponding to where maximal values of A_1 are observed. In addition, the values of A_1^{da} in the notched cross-section are noticeably smaller than those on the notch surfaces. This finding suggests that macro-cracks may initially appear on the exterior of the specimen and then propagate to the interior, leading to final failure caused by a mixed damage mechanism under low positive stress states ($0 \leq \eta \leq 0.33$). Moreover, the maximum values of A_1^{da} exhibit a decreasing trend with an increasing number of loading cycles. A similar trend is also observed in the magnitude of A_1, as shown in Fig. 4. In addition, the positions where numerically predicted maximum values appear in the notched cross-section alter from the middle to the edge, as observed in Fig. 6. Also, this observation is similar to the localization of the plastic strain in the notched cross-sections. In conclusion, these four experiments induce very similar stress triaxialities. It indicates that the evolution of damage and fracture is influenced by the loading patterns.

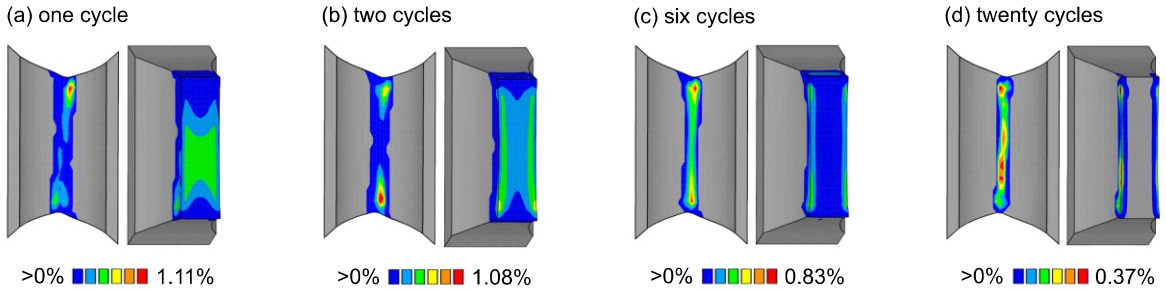

Figure 6: Numerically predicted the first principal damage strains A_1^{da} on the notch surfaces and notched cross-sections.

Fig. 7 shows the fracture lines and scanning electron microscopy (SEM) images for different loading paths. Both micro-voids and micro-shear-cracks are visible in the SEM images. It confirms that the mixed damage mechanism, due to the growth of micro-voids and micro-shear-cracks, is caused by low positive stress triaxialities. Experiments with one loading cycle show fewer large micro-defects and more micro-shear-cracks than other loading cases. Furthermore, the micro-defects are more densely distributed in experiments with twenty loading cycles than in others. As Wei et al. [12] pointed out, metallographic analysis reveals different evolutions under various loading patterns. Therefore, future work is recommended to analyze changes in the number and area of micro-defects with different loading cycles.

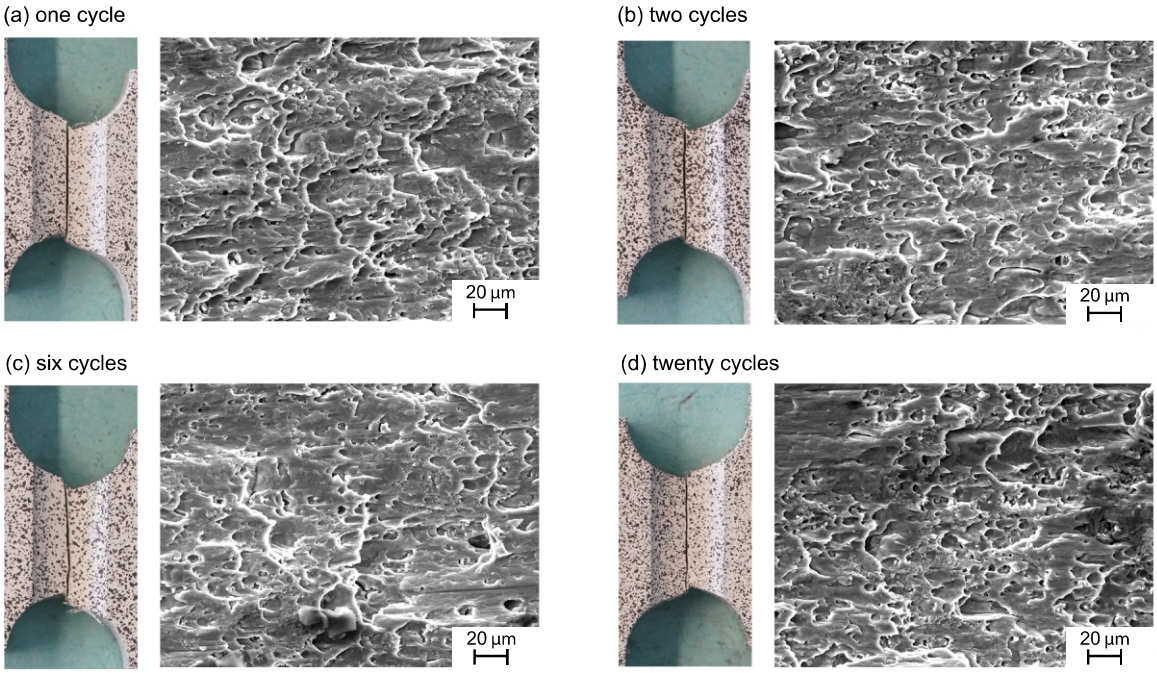

Figure 7: Fracture lines on the notch surfaces and scanning electron microscopy images taken from the fractured notched cross-sections.

5 Conclusions and discussion

The experimental and numerical results demonstrate different mechanical responses under low-cycle cyclic loading conditions in the macro- and micro-levels. Specimens failed at smaller first principal strains as the number of loading cycles increased. Experimental force–displacement curves align closely with each other within the loading process for experiments with six and twenty loading cycles, with maximum forces during the positive loading patterns changing only slightly. However, the current material model shows limitations in modeling the hardening changes after several reverse loading patterns. Based on the current results, it is suggested to further reduce the plastic deformations before the first reverse loading point and then impose a larger number of loading cycles to more comprehensively study the influence of low-cycle cyclic loading conditions on damage and fracture behavior. In addition, it is also recommended to apply different preloads with shear cyclic loading to generate a wide range of stress triaxialities, enabling the study of the influence of loading modes on damage and fracture behavior.

Acknowledgment

The project has been funded by the Deutsche Forschungsgemeinschaft (DFG, German Research Foundation) – project number 322157331, this financial support is gratefully acknowledged. The SEM images of the fracture surfaces presented in this paper were performed at the Institut für Werkstoffe im Bauwesen, University of the Bundeswehr Munich and the support of Wolfgang Saur is gratefully acknowledged.

REFERENCES

[1] L. Borrego, L. Abreu, J. Costa, J. Ferreira, Analysis of low cycle fatigue in AlMgSi aluminium alloys, Eng. Fail. Anal. 11 (5) (2004) 715–725.

[2] Y. Murakami, K. Miller, What is fatigue damage? A view point from the observation of low cycle fatigue process, Int. J. Fatigue 27 (8) (2005) 991–1005.

[3] Y. Shi, M. Wang, Y. Wang, Experimental and constitutive model study of structural steel under cyclic loading, J. Constr. Steel Res. 67 (8) (2011) 1185-1197.

[4] M. Algarni, Y. Bai, M. Zwawi, S. Ghazali, Damage evolution due to extremely low-cycle fatigue for Inconel 718 alloy, Metals 9 (10) (2019) 1109.

[5] A. M. Kanvinde, G. G. Deierlein, Cyclic void growth model to assess ductile fracture initiation in structural steels due to ultra low cycle Fatigue, J. Eng. Mech. 133 (6) (2007) 701–712.

[6] P.-O. Bouchard, L. Bourgeon, H. Lachapèle, E. Maire, C. Verdu, R. Forestier, R. E. Logé, On the influence of particle distribution and reverse loading on damage mechanisms of ductile steels, Mater. Sci. Eng., A 496 (1-2) (2008) 223–233.

[7] G. Z. Voyiadjis, S. H. Hoseini, G. H. Farrahi, A plasticity model for metals with dependency on all the stress invariants, J. Eng. Mater. Technol. 135 (1) (2013) 011002.

[8] Z. Wei, M. Zistl, S. Gerke, M. Brünig, Analysis of ductile damage and fracture under reverse loading, Int. J. Mech. Sci. (2022) 107476.

[9] H. Wu, C. Zhang, H. Yang, X. Zhuang, Z. Zhao, Extended Gurson-Tvergaard-Needleman model considering damage behaviors under reverse loading, Int. J. Mech. Sci. 272 (2024) 109196.

[10] Z. Wei, S. Gerke, M. Brünig, Damage and fracture behavior under non-proportional biaxial reverse loading in ductile metals: Experiments and material modeling, Int. J. Plast. 171 (2023) 103774.

[11] Z. Wei, S. Gerke, M. Brünig, Numerical analysis of non-proportional biaxial reverse experiments with a two-surface anisotropic cyclic plasticity-damage approach, Comput. Methods Appl. Mech. Eng. 419 (2024) 116630.

[12] Z. Wei, S. Gerke, M. Brünig, Ductile damage and fracture characterizations in bi-cyclic biaxial experiments, Int. J. Mech. Sci. (2024) 109380.

[13] A. L. Gurson, Continuum theory of ductile rupture by void nucleation and growth: part I—yield criteria and flow rules for porous ductile media, J. Eng. Mater. Technol. 99 (1) (1977) 2–15.

[14] V. Tvergaard, A. Needleman, Analysis of the cup-cone fracture in a round tensile bar, Acta Metall. 32 (1) (1984) 157–169.

[15] I. A. Khan, A. A. Benzerga, A. Needleman, A shear modified enhanced Gurson constitutive relation and implications for localization, J. Mech. Phys. Solids 171 (2023) 105153.

[16] J.-L. Chaboche, G. Rousselier, On the plastic and viscoplastic constitutive equations—Part I: rules developed with internal variable concept, J. Pressure Vessel Technol. 105 (2) (1983) 153–158.

[17] S. Gerke, Z. Wei, M. Brünig, Experiments on low-cycle ductile damage and failure under biaxial loading conditions, Exp. Mech. (2024) 1–16.

[18] K. Hayakawa, S. Murakami, Y. Liu, An irreversible thermodynamics theory for elastic-plastic-damage materials, Eur. J. Mech. A Solids 17 (1) (1998) 13–32.

[19] M. Brünig, An anisotropic ductile damage model based on irreversible thermodynamics, Int. J. Plast. 19 (10) (2003) 1679–1713.

[20] N. Ohno, Y. Kachi, A constitutive model of cyclic plasticity for nonlinear hardening materials, J. Appl. Mech. 53 (2) (1986) 395–403.

[21] V. Okorokov, Y. Gorash, D. Mackenzie, R. van Rijswick, New formulation of nonlinear kinematic hardening model, Part II: Cyclic hardening/softening and ratcheting, Int. J. Plast. 122 (2019) 244–267.